Broadband polarization insensitivity and high detection efficiency in high-fill-factor superconducting microwire single-photon detectors: supplementary material

DILEEP V. REDDY[1,2,*], NEGAR OTROOSHI[1,2], SAE WOO NAM[2], RICHARD P. MIRIN[2], AND VARUN B. VERMA[2]

[1] *Department of Physics, University of Colorado, Boulder, Colorado 80309, USA*
[2] *National Institute of Standards and Technology, Boulder, Colorado 80305, USA*
* dileep.reddy@nist.gov

Compiled April 3, 2022

This document provides supplementary information to "Broadband polarization insensitivity and high detection efficiency in high-fill-factor superconducting microwire single-photon detectors." The identification of commercial instruments in this document does not imply recommendation or endorsement by the National Institute of Standards and Technology.

---

1. DEVICE DESIGN AND FABRICATION
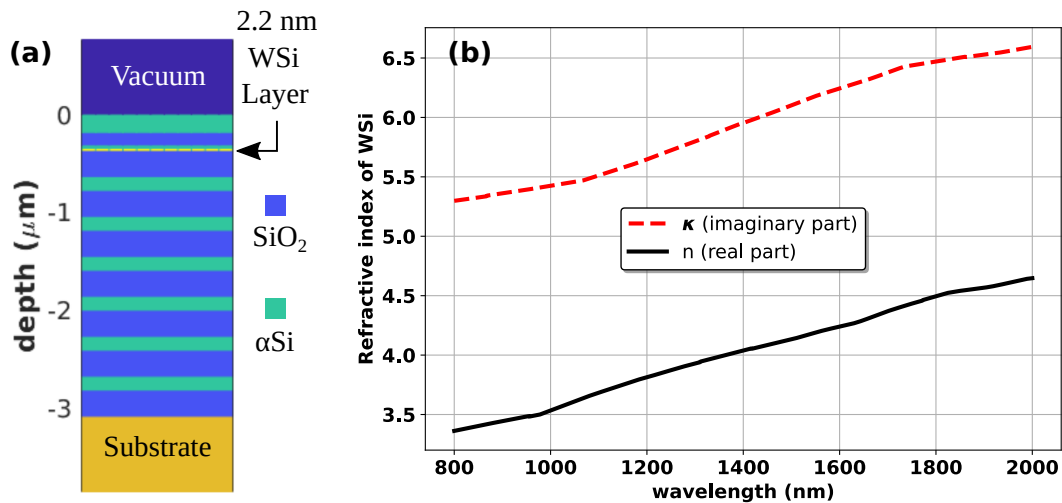
Fig. S1. (a) Vertical slice of the Bragg-reflector-based optical stack. The microwire is buried beneath a three-layer antireflection coating. Light is incident from the top. (b) The refractive index estimate of the 2.2 nm thick WSi layer, estimated from transmittance and reflectance measurements from a sputtered deposit on a UV-fused silica wafer.

The Bragg-reflector based optical stack [1] consists entirely of two dielectric materials with an index contrast, and the sputtered superconducting thin film (with an ultra-thin capping layer of amorphous silicon to prevent oxidation). We deposited all of our dielectric layers in both the Bragg reflector and the antireflection coating using a Plasma-enhanced chemical vapor deposition (PECVD) tool. The materials used are silicon dioxide (SiO_2) and amorphous silicon (αSi). Their refractive indices were measured as 1.453 ± 0.0005 (SiO_2) and 2.735 ± 0.0005 (αSi) at a wavelength of 1550 nm. The

refractive index of the 2.2 nm thick tungsten silicide (WSi) layer was estimated to be $(n, \kappa) = (4.19, 6.18)$ (see fig. S1(b)) using transmittance and reflectance measurements off of a deposited layer on UV-fused silica.

With an ideal Bragg reflector composed of thirteen alternating layers of SiO_2 and Si (starting with SiO_2, see fig. S1(a)) with optical thicknesses of $\lambda/4$ at 1550 nm, we used rigorous coupled-wave analysis (RCWA) to optimize a three-layer antireflection (AR) coating to minimize back-reflection of vertically incident light at 1550 nm. For a microwire grating of width 0.51 μm and an inter-wire gap of 50 nm, the optimum AR coating was 28 nm (αSi), 123 nm (SiO_2), and 183.5 nm (αSi), from bottom to top.

The layer-thickness errors at the center of a 76.2 mm diameter substrate wafers were sub-1 nm between deposition runs on the tool. However, the layer thicknesses were not uniform across the wafer due to the tool's inherent design. The three-layer AR coating optimum was sought in a parameter regime where increase in the top-most Si-layer thickness moved the minimum-reflectance wavelength higher with negligible change in the reflectance at said wavelength. Therefore, during fabrication, we deliberately undershot the thickness of the final AR-coating layer. This allowed us to repeatedly transfer the wafer in the cleanroom between the PECVD tool and a Filmetrics reflectometry tool. The reflectance of a 10 μm spot focussed on the top surface of the vertical stack was sequentially monitored as short, corrective depositions to the top layer were made. This method allowed for easy compensation for all of the collective fabrication errors that may have occurred in all the previous steps. However, due to the nonuniformity of the dielectric layer thicknesses across the wafer, the optimum wavelength for different devices depended on the die location on the wafer (see fig. S2). Our devices were placed on 4 mm × 6 mm dies, and were optimized for 1550 nm only near the center of the wafer.
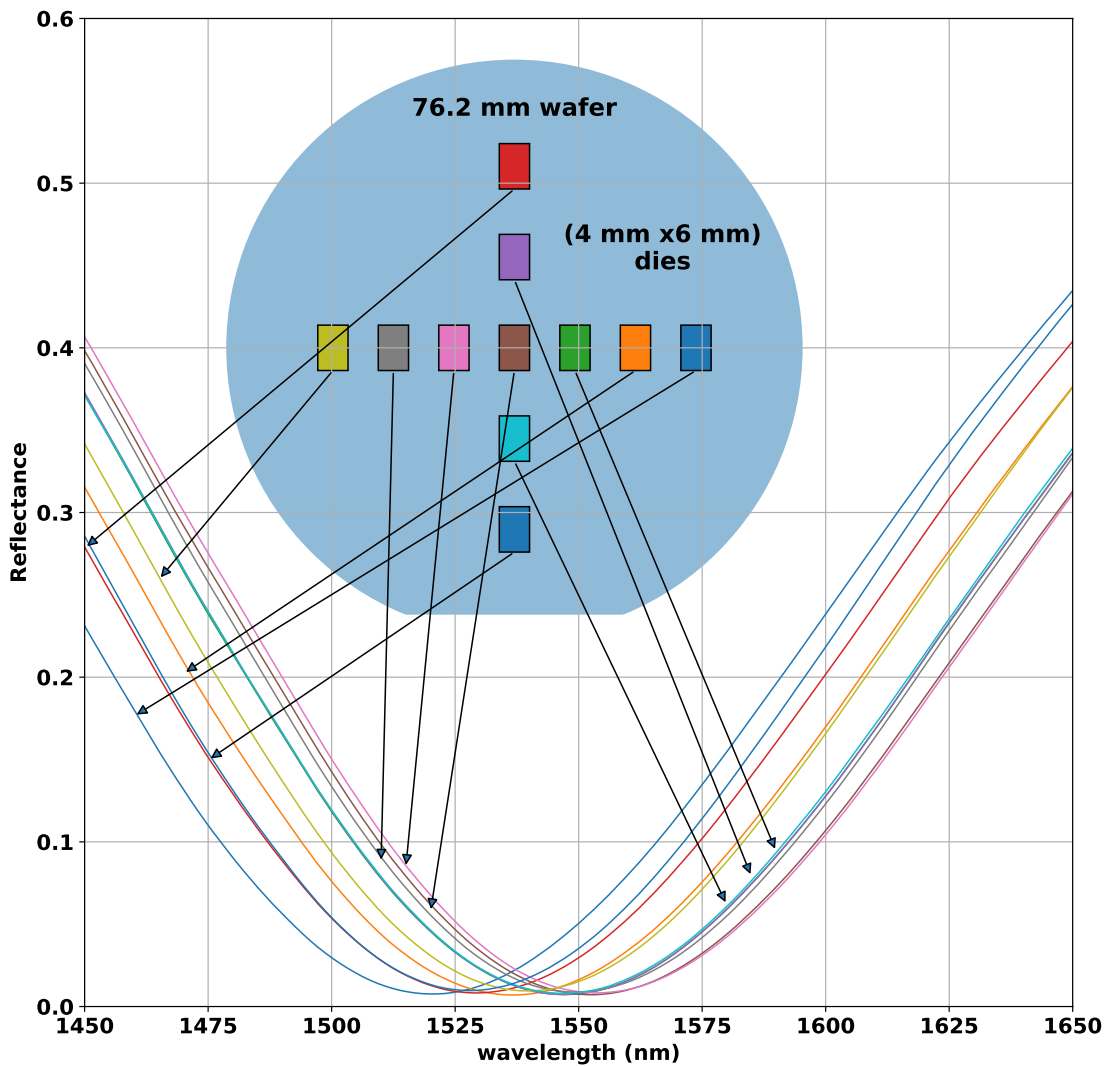
Fig. S2. Reflectance of a vertically incident 10 μm spot focused on the top surface of the devices (measured using a Filmetrics reflectometry tool). The plots for various die locations on the 76.2 mm wafer indicate that the devices on the wafer's periphery ended up optimized for absorption at shorter wavelengths.

The candelabra-meander pattern was drawn using the `python` CAD-layout library `phidl` [2]. A superconducting wire "goes normal" when the current density exceeds a certain value related to its depairing current. When a conductive path in any current-biased thin film bends, the current crowds towards the inner radius (see main manuscript), meaning that the current density is no longer uniform across the width of the conductive path like in its straight segments. The current density at the inner radius can exceed the current density in the straight segments by an amount related to the width of the path and the bend radius. In superconducting wires, these regions can also be a significant source of dark counts [3].

For a hairpin bend, where in the direction of the path turns by 180 degrees, for the current density at the bend to not exceed that in the straight segments, the bend-geometry must match the current-distribution contour lines, and the local fill factor must be ≤ 0.33 [4, 5]. The `phidl` library contains built-in methods for plotting optimized 90-degree and 180-degree turns for any given wire width. These were utilized to create the candelabra meander (see fig. S3(a)), which allows for high fill factors in a designated active area by moving all the turns and low-fill-factor hairpin bends to the outside of it [5]. This pattern was written into a PMMA resist coating using an e-beam writer. It was developed in cold (5°C) 1:3 MIBK:IPA solution, and the pattern was then etched into the WSi layer using an SF_6-based reactive-ion etch recipe. Figures S3(b) and S3(c) show SEM images of the pattern after it has been etched into WSi.
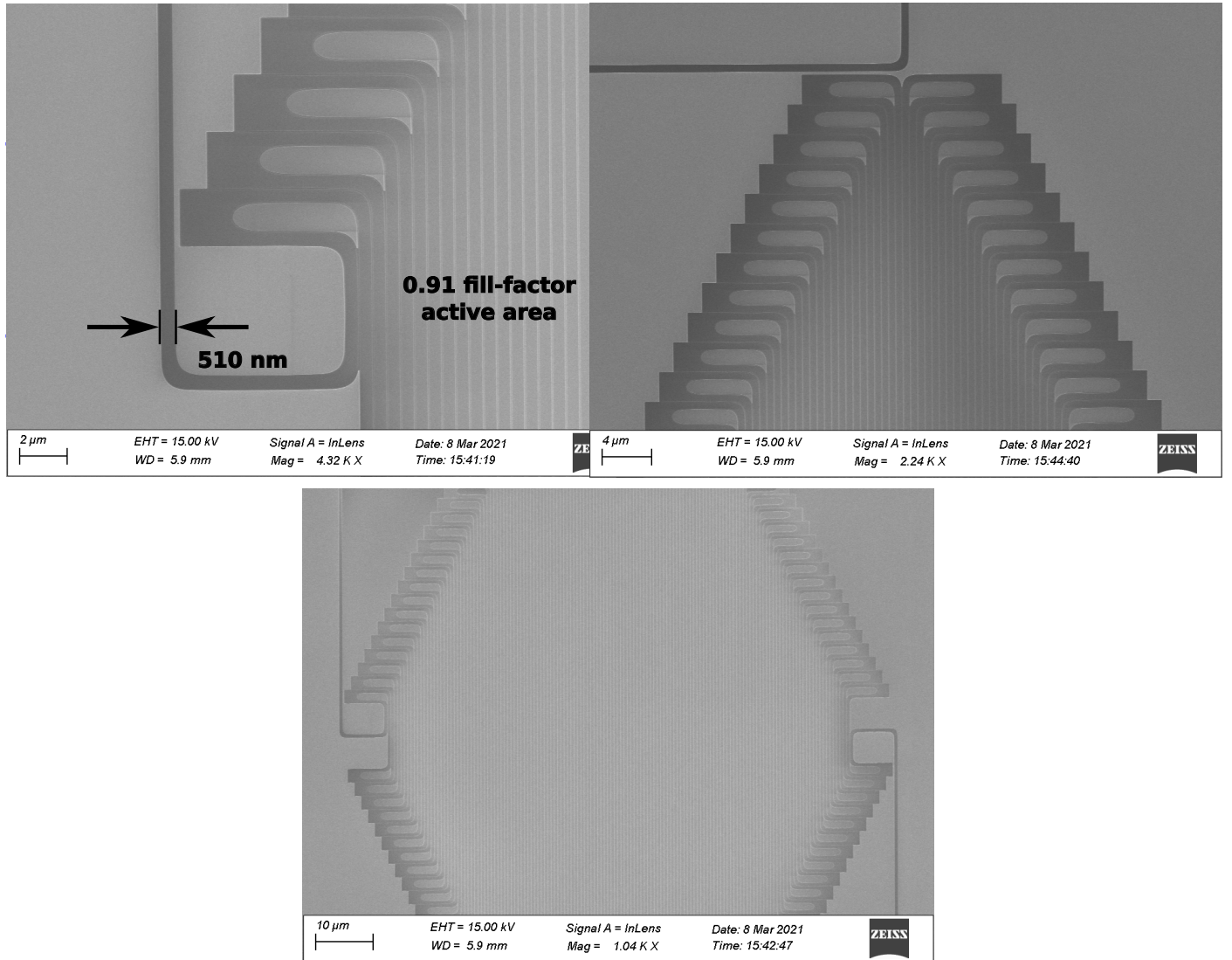
Fig. S3. SEM images of the candelabra meander etched into WSi.

All the gold pads (50 nm electrical terminals, and 100 nm spacer layer) and the palladium-gold speed-up resistor [1] were deposited using an LOR3A+SPR660 photolithographic lift-off process. They were all sandwiched between 2 nm layers of titanum for adhesion. Two 100-nm thick gold spacers on top of the stack on either side of the active area (separated by 120 μm) prevented the fiber-pigtail/ceramic-ferrule front faces from making contact and damaging the optical stack in the self-aligning fiber package [6]. This ensured the presence of vacuum/air between the optical stack

and the AR-coating on the fiber face.

2. EFFICIENCY MEASUREMENT PROCEDURE AND ERROR ANALYSIS

With multiple groups now reporting near-unity detection efficiencies for SNSPDs/SMSPDs [1, 7, 8], the need has arisen to standardize and tighten the procedures for the same. While there are multiple approaches to estimating detector efficiency [9, 10], they all rely on one or more power meters which are well calibrated to report accurate readings at known wavelengths, power-meter range settings, and light levels [11]. The method we have developed and present in detail here requires two power meters with low electrical noise. Only one of these are required to be calibrated for accurate readings at a single classical light level and range (gain) setting at all desired wavelengths. This method was developed specifically for accessibility and ease of implementation.

Our procedure estimates the SDE as the ratio of the time-averaged number of detection events registered from the device to the expected count rate, with light from a highly-attenuated continuous-wave laser as the input. The expected count rate is calculated by measuring the laser power without optical attenuation using a calibrated power meter, and then estimating the attenuation applied. Optical attenuation estimation requires power measurements both with and without the attenuation applied. No power meter designed for classical light-levels is sensitive to light at the low powers necessary for testing single-photon detectors. Therefore, multiple modular optical attenuators are used, with each one applying a fraction of the required total attenuation. Calibrating these modular attenuators individually involves measuring and comparing optical powers that are several orders of magnitude apart. The power meter used for this purpose will need to operate at different range/gain settings to measure and compare such optical powers. Both the nonlinear response of this power meter within a range setting, as well as response discontinuities across contiguous range-setting changes, are estimated using a nonlinearity-correction step. And lastly, an optical switch in the system is also calibrated using two power meters in the same range setting, one of which has been calibrated in that range setting to act as an absolute power reference.

The chief advantage of this procedure is that it only requires one optical element (the calibrated power meter) to have been externally characterized at one classical light level (and range setting) to act as a reference. All the other optical elements (switch, attenuators, other power meters) are calibrated live. Additionally, the same experimental setup serves for both device SDE measurement and optical-element calibration. The only physical modification to the setup required during the procedure is the fiber-splicing involved in routing the prepared light to the device under test (DUT) instead of the calibrated power meter.
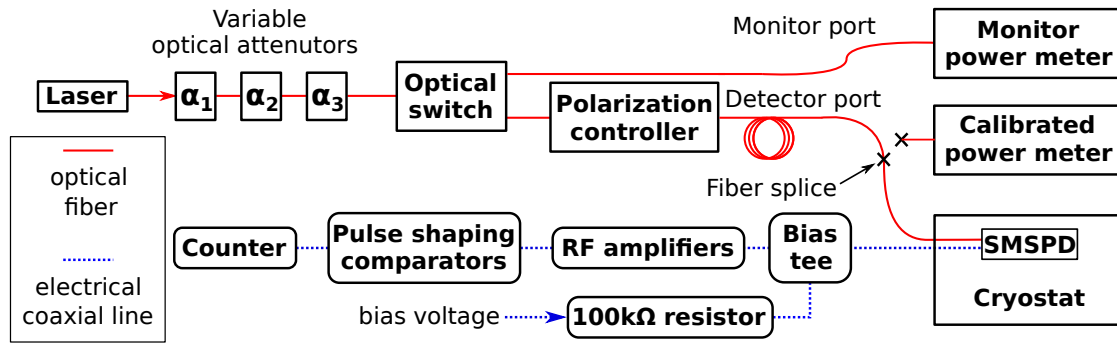
Fig. S4. SDE measurement setup, illustrating the optical calibration and input state preparation, as well as the electrical biasing and readout circuitry. SMSPD stands for superconducting microwire single-photon detector.

The full schematic of the experimental setup is shown in fig. S4. The optical components used are a tunable, continuous-wave laser (`Ando AQ8201-13B`), three all-fiber tunable optical attenuators with at least one equiped with a monitoring port (`Ando AQ8201-33(M)`), an optical switch (`Ando AQ8201-422`), a monitoring power meter (MPM) (`Ando AQ8201-22`), a NIST-calibrated power meter (CPM) (`Agilent HP81533B` with `InGaAs` optical head), and a programmable polarization controller. For efficiency measurements, a `FiberControl MCP-01` all-fiber polarization controller was used. For sampling the Bloch sphere for all input polarization states, it was swapped with a free-space `Hewlett-Packard HP8169A` polarization controller. The laser, attenuators, optical switch, and the MPM were all slotted into an `Andorack AQ8201A` mainframe with a `GPIB` control interface. They are all daisy-chained optically using black-jacketed `FC/APC` patch chords. The CPM is "perpetually" attached to an `SMF28e+` fiber pigtail with the same AR-coating on its ceramic front face as the ones inserted into the SMSPDs. This fiber pigtail is identical to the one used during CPM calibration at NIST.

The two output routes of the optical switch are labeled the monitor port, and the detector port (see fig. S4). The polarization controller is attached to the output route meant for the devices under test. The fiber port at the output of

the polarization controller is labeled the detector port. This fiber port is an exposed, bare `SMF28e+` fiber which can be spliced either to a fiber pigtail plugged into the CPM (as is done during the switch calibration step, detailed below), or to the fiber optically coupled to the DUT. The system detection efficiency (SDE) is defined as the probability of the detector producing a detection event given that a photon is present in the optical mode exiting the detector port. A bad (lossy) fiber splice into the DUT fiber will underestimate the SDE. A bad fiber splice into the CPM during the switch calibration step will overestimate the SDE. Special care is taken to achieve the best fiber splice into the CPM (through repeated attempts) for the switch calibration step.

The electrical components in the setup are a low-noise programmable voltage source (`Keithley 213`), a pulse counter (`SRS SR400`), a digital multimeter (`Keithley 199`) (not shown) used to monitor the voltage drop across the DUT, room temperature low-noise `Mini-Circuits` RF amplifiers (`ZFL500LN+`, `ZFL1000LN+`), a standard `Mini-Circuits` bias tee, a custom comparator circuit, and assorted inline resistors and low-pass filters (not shown). As mentioned in the main manuscript, the DUTs are quasi-current-biased using the voltage source and a 100 kΩ series resistor.

A. Calibrated power meter readings

The NIST-calibrated `InGaAs` optical head and `HP81533B` pair were calibrated at specific near-infrared wavelengths at a light level of 100 μW (see fig. S5(a)). The CPM reading of 100 μW taken with range setting of -10 dBm is to be divided by the calibration factor ($CF_{\mathrm{CPM}}(\lambda)$) to recover the actual power. Although the company datasheet lists a standard deviation of 2.5%, the calibration factors for this specific CPM were estimated to better than 0.14% (see errorbars in fig. S5(a)). Throughout error analysis, we will use the conservative value of $\sigma_{\mathrm{CPM}}/CF_{\mathrm{CPM}}(\lambda) = 0.14\%$ $\forall \lambda$ for relative standard uncertainty. NIST offers additional types of calibrations, such as nonlinearity correction for different range settings and light levels. Our method does not rely on these.
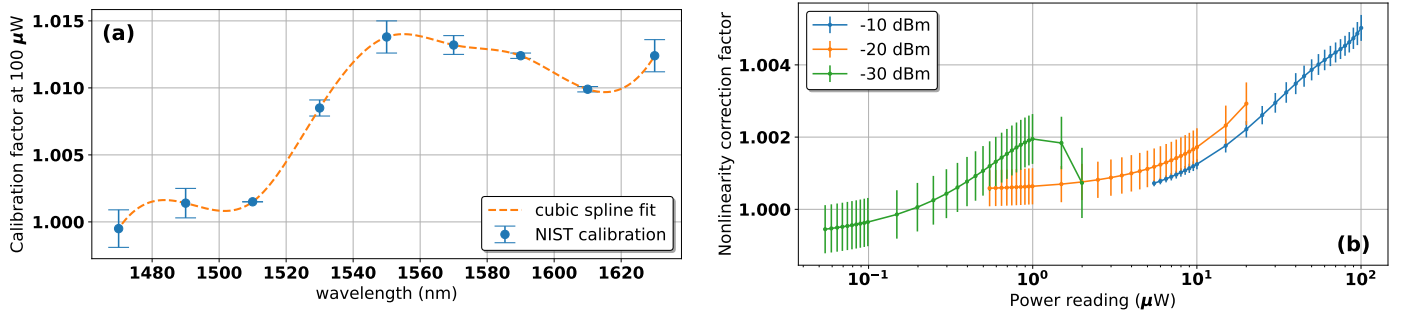
Fig. S5. (a) NIST-provided calibration factor ($CF_{\mathrm{CPM}}(\lambda)$) for the calibrated power meter at power reading of 100 μW. (b) The nonlinearity correction factors ($CF_{\mathrm{NL}}(\lambda, r, v)$) versus power-meter reading (v) for the monitoring power meter estimated for various range settings at $\lambda = 1550$ nm.

B. Monitoring power meter nonlinearity correction

The nonlinearity correction factor ($CF_{\mathrm{NL}}(\lambda, r, v)$, where v is the power-meter reading, r is the range setting, and λ the wavelength) is estimated for the MPM by measuring its power readings in the power range of $P_{\mathrm{MPM}} = 1\mathrm{nW} - 100\mu\mathrm{W}$ and all range settings ($r \in (-10, -20, -30, -40, -50, -60)$ dBm) [12]. For this, two of the attenuators are used (the third one is held at "0 dB" setting) and the optical switch is set to route the light to the MPM. No assumptions are made about the precise value of the attenuation applied, but attenuator repeatability is assumed. The procedure for these measurements is shown in algorithm S1.

Algorithm S1 is run at every desired wavelength. It records the MPM power readings at various light levels (dictated by the attenuator settings). Of the two attenuators varied, one ($att1$) is used in a range of settings to sweep the power reading monotonically, while the other ($att2$) is used as a binary on/off device by switching its settings between nominal values of "0 dB" and "3 dB". The actual amount of optical attenuation applied by the "3 dB" setting relative to the "0 dB" setting is an unknown (but to be fit) parameter τ. The objective of algorithm S1 is two-fold, namely: (a) to record an array of MPM readings over a multitude of $att1$ settings at every MPM range setting both with (V_τ) and without (V) the attenuation τ applied by $att2$, and (b) to record several MPM readings with the same $att1$ and $att2$ settings across contiguous MPM range settings. Figure S6(a) shows the readings taken at 1550 nm for two range settings. The points that overlap in attenuator settings will be used to compute the range discontinuity.

The nonlinearity correction for the MPM has two components. The first corrects for the nonlinear response to incident power within a range setting, and the other corrects for a discontinuity in readings for the same incident power across a
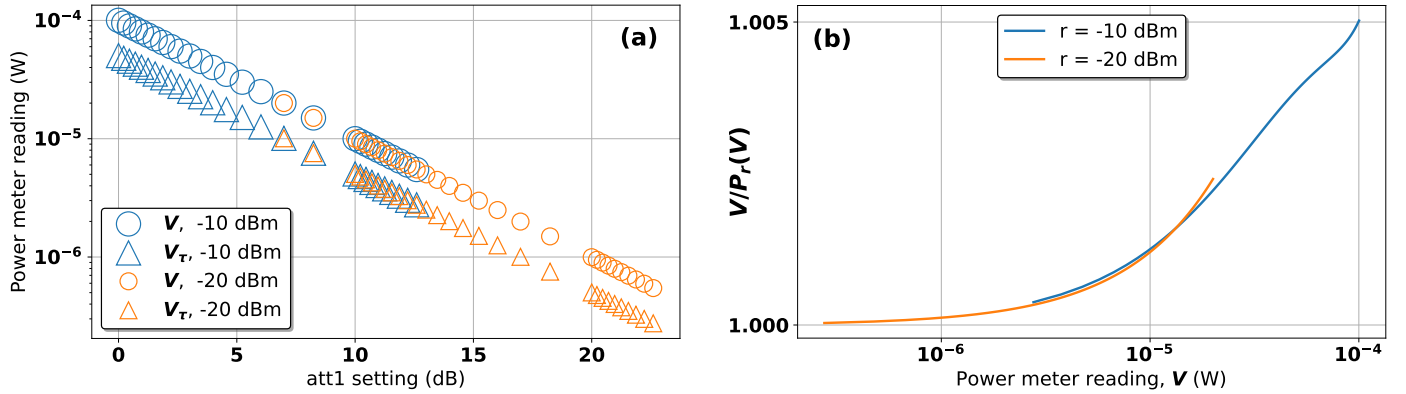
Algorithm S1. Nonlinearity factor raw power meaurements

```
 1: procedure CONSOLE_NONLINEARITY(pm, att1, att2, out)        ▷ pm ≡ MPM, att(1, 2) ≡ attenuators, out ≡ file
 2:     N ← 10                                                            ▷ Number of reads at each setting
 3:     xlist ← [20, 15]
 4:     xlist.append(arange(10, 0.9, −0.5))                                   ▷ 10 to 0.9 in steps of -0.5
 5:     xlist.append(arange(0.95, 0.5, −0.5))                                 ▷ 0.95 to 0.5 in steps of -0.5
 6:     base_array ← round(10 − 10 ∗ log₁₀(xlist))
 7:     base_array ← base_array − min(base_array)
 8:     att_setting ← {}                                                   ▷ initialize empty dictionary
 9:     for rng ∈ [−10, −20, −30, −40, −50, −60] do                            ▷ rng ≡ range setting
10:         att_setting[rng] ← base_array − (rng + 10) − 3                        ▷ 3 is an offset
11:
12:     for rng ∈ [−10, −20, −30, −40, −50, −60] do
13:         pm.set_range(rng)                                             ▷ Set MPM range setting to rng
14:         pm.zero()                                                         ▷ Zero the MPM
15:         for α ∈ att_setting[rng] do
16:             att1.set_att(α)                                         ▷ Set attenuation setting on att1 to α
17:             for att_step ∈ [0, 3] do
18:                 att2.set_att(att_step)                              ▷ Set attenation setting on att2 to att_step
19:                 for i ← 1 to N do                                          ▷ Iterate N times
20:                     power ← pm.get_power()
21:                     out.write(α, att_step, rng, power)    ▷ Record settings and power readings from MPM into file
```


Fig. S6. (a) MPM Power readings (V, V_τ) under two range settings measured at a range of attenuation settings for 1550 nm light for nonlinearity calibration (see algorithm S1). (b) The ratio of the readings (V) to the polynomial fit $(P_r(V))$ for two range settings $r \in \{−10, −20\}$ dBm.

change in range setting. To achieve the former, we use the python `lmfit` library and model the function that maps the MPM readings (at range setting r) to the linearized power as a polynomial $P_r(V)$, defined as

$$P_r(V) = V + \sum_{k=2}^{N_r} b_k^{(r)} V^k, \tag{S1}$$

where N_r is the order of the polynomial. We can then determine the coefficients of the polynomial $\{b_k^{(r)}\}$ and the unknown attenuation τ by solving for

$$P_r(V_\tau) − \tau P_r(V) = 0, \forall r \in \{−10, −20, −30, −40, −50, −60\} \text{ dBm}, \tag{S2}$$

where V_τ and V are the readings recorded at range-setting r. This polynomial fit is performed by minimizing the residual simultaneously at all the range settings recorded. The choice of what order of polynomial to fit for at each range setting (N_r) is made by minimizing the reduced chi-square goodness-of-fit metric over the full range of choices between 1 and 5 for each range-setting r. Figure S6(b) shows the polynomial fits made using the data in fig. S6(a). Note the discontinuity across the change in range setting in the overlapping region.

For the second aspect of nonlinearity correction, namely, range discontinuity, we consider the MPM readings recorded at the same combined ($att1$, $att2$) attenuation settings across two contiguous range settings r and $r + 10$ dBm. These readings ($\overline{V}_r$) will be a subset of the full record of MPM readings from algorithm S1. These readings are then used to compute an average ratio of polynomial-fit-corrected readings across ranges r and $r + 10$ dBm, giving as a value denoted by $RF_{\mathrm{NL}}(\lambda, r)$. To get the full nonlinearity correction $CF_{\mathrm{NL}}(\lambda, r, v)$ for MPM reading v at range setting r, we first commulatively multiply $RF_{\mathrm{NL}}(\lambda, r')$ for all $r' \in \{r, r + 10, r + 20, ..., -20\}$ dBm, and we then multiply that to $v/P_r(v)$. More explicitly,

$$RF_{\mathrm{NL}}(\lambda, r) = \left\langle \frac{P_r(\overline{V}_r)}{P_{r+10}(\overline{V}_{r+10})} \right\rangle_{(att1,att2)}, \quad CF_{\mathrm{NL}}(\lambda, r, v) = \frac{v}{P_r(v)} \times \left(\prod_{r'=r}^{-20\,\mathrm{dBm}} RF_{\mathrm{NL}}(\lambda, r') \right). \tag{S3}$$

The full nonlinearity correction is applied to any MPM reading v at range setting r by dividing the reading by $CF_{\mathrm{NL}}(\lambda, r, v)$. The range setting of $r = -10$ dBm is the highest reached in this experiment, and is the one at which the calibration factor for the CPM is known. Hence we only account for range discontinuities up to $r = -10$ dBm ($RF_{\mathrm{NL}}(\lambda, r = -10\,\mathrm{dBm}) = 1$). Figure S5(b) plots the nonlinearity correction factor for the MPM over three range settings for 1550 nm light. For convenience's sake, we will omit the third argument (v) in CF_{NL} when denoting the nonlinearity correction factor in error analysis.

The standard ($k = 1$) uncertainties in the nonlinearity correction factors for range-setting -30 dBm were between 0.061% and 0.075% over the wavelengths considered. For this error budget calculation, we will use the conservative maximum value of $\sigma_{\mathrm{NL}}/CF_{\mathrm{NL}}(\lambda, r, v) = 0.075\%$ $\forall \lambda, \forall v$ for the relative standard uncertainty.

C. Optical switch calibration

The optical switch is calibrated at classical light levels of around 100 μW at desired wavelengths using both the CPM and MPM. The detector port is spliced into the fiber pigtail coupled to the CPM (see fig. S4), and the switch is alternatingly "flipped" to route the power to either the monitor port or the detector port while several power readings are recorded from both power meters. The range settings for both power meters are set to -10 dBm, and the attenuators are all set to a zero-attenuation setting. This step was carried out with the all-fiber `MCP-01` polarization controller only.
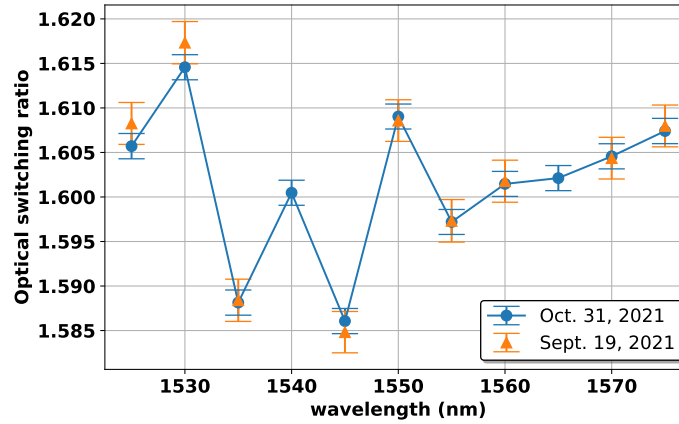
Fig. S7. The switching ratio versus wavelength of the optical switch measured with classical light levels (100 μW) using the calibrated and the monitor power meters. The switching ratio did not change much over 40 days (see legend). The switching ratios used for SDE estimates were measured just before and after the efficiency measurement runs.

The switching ration $R_{\mathrm{SW}}(\lambda) = P_{\mathrm{CPM}}(\lambda)/P_{\mathrm{MPM}}(\lambda)$ is plotted in fig. S7. This ratio was calculated before every run which required splicing a fiber to a DUT. As can be seen in fig. S7, the ratio barely drifts over 30 days due to the temperature stability of the lab, and the mechanical stability of the setup. The relative standard uncertainty in the switching ratio was $\sigma_{\mathrm{SW}}/R_{\mathrm{SW}}(\lambda) \leq 0.14\%$ as the MPM readings were very stable at these light levels.

D. Attenuator calibration

The optical attenuators were calibrated one at a time, meaning with the other two attenuators set to zero-attenuation setting. This allows for the light level reaching the MPM to be large enough for a valid read out with an appropriate range setting. For any given attenuator setting, the absolute amount of optical power exiting the detector-port fiber is $P_{\mathrm{DP}} = P_{\mathrm{MPM}}/R_{\mathrm{SW}}/CF_{\mathrm{CPM}}(\lambda)/CF_{\mathrm{NL}}(\lambda, r, P_{\mathrm{MPM}})$, where P_{MPM} is the power reading from the MPM at wavelength λ and range setting r. The absolute power is calculated with the attenuation setting (for the attenuator being calibrated) set to

both the zero-attenuation setting and the setting used in the DUT measurement. The ratio of the estimates of absolute power is equal to the true attenuation applied. It is assumed that the attenuations apply cummulatively when all three attenuators are set to a high-attenuation setting together.

Due to several factor cancellations, the R_{SW} and CF_{CPM} need not be used in attenuator calibration. The relative standard uncertainty for attenuator α_i is

$$\frac{\sigma_{\alpha_i}}{\alpha_i} = \sqrt{\left(\frac{\sigma_{\text{MPM}}}{P_{\text{MPM}}}\right)^2_{r=-10\text{ dBm}} + \left(\frac{\sigma_{\text{MPM}}}{P_{\text{MPM}}}\right)^2_{r=-30\text{ dBm}} + \left(\frac{\sigma_{\text{NL}}}{CF_{\text{NL}}(\lambda, r=-10\text{ dBm})}\right)^2 + \left(\frac{\sigma_{\text{NL}}}{CF_{\text{NL}}(\lambda, r=-30\text{ dBm})}\right)^2}. \quad \text{(S4)}$$

For a photon flux of 2×10^5 per second, the attenuation setting for all three attenuators was 31 dB, and the range setting on the MPM during attenuator calibration was -30 dBm, yielding a relative standard uncertainty of $\sigma_{\alpha_i}/\alpha_i = 0.2\%$.

This procedure (see algorithm S2) is performed every time the counts from the DUT are measured for efficiency estimation. The CPM is not used, and the detector port is spliced into the fiber coupled to the DUT during attenuator calibration. The optical switch is set to route the light to the MPM throughout this procedure.

Algorithm S2. Attenuator calibration

1: **procedure** CONSOLE_CAL($pm, att\_list, attval, rngval, out$) $\triangleright pm \equiv$ MPM, $att\_list \equiv$ attenuators, $attval \equiv$ attenuator value, $rngval \equiv$ range value, $out \equiv$ file
2:     $N = 5$ $\triangleright$ Number of measurements
3:     $init\_rng = -10$ $\triangleright$ Initial MPM range setting
4:     **for** $att \in att\_list$ **do**
5:         $att.set\_att(0)$ $\triangleright$ Set all attenuators to 0 dB
6:
7:     **for** $att \in att\_list$ **do**
8:         $pm.set\_range(init\_rng)$
9:         $att\_list.disable()$ $\triangleright$ Disable all attenuators
10:         $pm.zero()$ $\triangleright$ Zero the MPM
11:         $att\_list.enable()$ $\triangleright$ Enable all attenuators
12:         $powers \leftarrow \{\}$
13:         **for** $i \leftarrow 1$ **to** N **do** $\triangleright$ Iterate N times
14:             $powers.append(pm.get\_power())$
15:         $out.write(att\_list.get\_att(), powers, init\_rng)$ $\triangleright$ Write to file
16:         $att.set\_att(attval)$ $\triangleright$ Set attenuator att to $attval$
17:         $pm.set\_range(rngval)$ $\triangleright$ Change range of MPM
18:         $att\_list.disable()$ $\triangleright$ Disable all attenuators
19:         $pm.zero()$ $\triangleright$ Zero the MPM
20:         $att\_list.enable()$ $\triangleright$ Enable all attenuators
21:         $powers \leftarrow \{\}$
22:         **for** $i \leftarrow 1$ **to** N **do** $\triangleright$ Iterate N times
23:             $powers.append(pm.get\_power())$
24:         $out.write(att\_list.get\_att(), powers, rngval)$ $\triangleright$ Write to file
25:         $att.set\_att(0)$

E. System detection efficiency estimation

SDE measurements are done with the detector port spliced to the fiber coupled to the DUT. Since attenuator calibrations are integrated with this routine, the optical switch will be used to route the light to either the DUT or the MPM in different steps. The procedure is shown in algorithm S3. We record counts from the DUT while scanning the voltage bias applied. This is done under (a) "dark" circumstances to record the dark counts, and under "bright" circumstances (laser-light directed at DUT) (b) with polarization settings set to maximize the counts, and (c) with the polarization settings set to minimize the counts. The SDE measurements are only done with the MCP-01 all-fiber polarization controller, whose transmission loss is independent of polarization settings. The optical switch calibration, the MPM nonlinearity correction calibration (see algorithm S1), and the SDE counts measurement (see algorithm S3) for any wavelength can be performed in any order, but all three are essential for SDE estimation.

For an estimated absolute detector-port power of P_{DP} (with all three attenuators set to 'zero-attenuation' setting), and with the attenuations calibrated to be $(\alpha_1, \alpha_2, \alpha_3)$, the number of photons exiting the detector port per unit time with the attenuations applied would be

$$N_{\mathrm{photons}} = \frac{P_{\mathrm{DP}} \cdot \alpha_1 \cdot \alpha_2 \cdot \alpha_3 \times \lambda}{hc}, \tag{S5}$$

where hc/λ is the energy of a single photon at wavelength λ. The SDE at any given current bias is estimated by dividing the net count rate of the DUT by N_{photons}. The net count rate is defined as the difference between the time-averaged count rates ($\langle CR \rangle$) with the light routed to the DUT and the time-averaged dark-count rates ($\langle DCR \rangle$). The relative uncertainty in SDE is expressible as

$$\frac{\sigma_{\mathrm{SDE}}}{SDE} = \sqrt{\frac{\sigma_{\mathrm{CR}}^2 + \sigma_{\mathrm{DCR}}^2}{(\langle CR \rangle - \langle DCR \rangle)^2} + \left(\frac{\sigma_{\mathrm{DP}}}{P_{\mathrm{DP}}}\right)^2 + \sum_{i=1}^{3} \left(\frac{\sigma_{\alpha_i}}{\alpha_i}\right)^2}, \tag{S6}$$

where the relative uncertainty in the estimated detector-port power is in turn

$$\frac{\sigma_{\mathrm{DP}}}{P_{\mathrm{DP}}} = \sqrt{\left(\frac{\sigma_{\mathrm{MPM}}}{P_{\mathrm{MPM}}}\right)^2 + \left(\frac{\sigma_{\mathrm{SW}}}{R_{\mathrm{SW}}}\right)^2 + \left(\frac{\sigma_{\mathrm{CPM}}}{CF_{\mathrm{CPM}}}\right)^2 + \left(\frac{\sigma_{\mathrm{NL}}}{CF_{\mathrm{NL}}}\right)^2}. \tag{S7}$$

The standard deviations for the count rate (σ_{CR}) and the dark-count rate (σ_{DCR}) are merely the Poisson standard deviations ($\sqrt{\langle CR \rangle}$ and $\sqrt{\langle DCR \rangle}$ respectively). The numerical standard deviations of the ten consecutive measurements (see algorithm S3) made at every current bias was found to be slightly less than the expected Poisson value. We will be using the quadrature sum of the numerical standard deviation and the Poisson standard deviation in our error analysis. Table S1 tabulates the relative uncertainties estimated for the other variables.

Table S1. Error budget

Source	Symbol	Standard ($k = 1$) relative uncertainty
Calibration factor	$CF_{\mathrm{CPM}}(\lambda)$	0.14%
Nonlinearity correction	$CF_{\mathrm{NL}}(\lambda, r = -30\ \mathrm{dBm})$	0.075%
Optical switching ratio	R_{SW}	0.14%
Optical attenuation	$\alpha_i, i \in \{1, 2, 3\}$	0.2%
Monitor power meter	$P_{MPM}\vert_{r=-30\ \mathrm{dBm}}$	0.1%
SDE @ 2×10^5 counts per second		0.46%
SDE @ 1×10^5 counts per second		0.51%

Many of the source terms in table S1 are composites of other source terms, and consequently inherit their errors. Using these conservative errors, the $k = 1$ relative uncertainty for our SDE estimates comes to 0.46% at count rates of 2×10^5 per second, and 0.51% at count rates of 1×10^5 per second. Note that in the data presented in the main manuscript, all the errors for SDE were programmatically computed using the `uncertainties` python library, which automatically tracks the error propagation (with covariances for any calculated fit parameters) through arithmetic operations.

All the optical components used in SDE estimation were measured to be stable over a period of 10 hours. The laser had a built-in power setting and a wavelength setting. We set the power setting and let it equilibrate for over 24 hours before beginning any measurements. Changing the wavelength changed the power, but did not introduce any additional drift. As a precaution the wavelength changes were also dwelled on for half an hour of equilibration. Figure S8(a) shows the laser power drift (on the MPM) after a power setting was set and the laser was allowed to equilibrate for 17 hours. The typical duration for a complete wavelength scan per DUT was 7 hours, a large portion of which was meant for equilibration dwells for wavelength setting changes. Figure S8(b) shows the Allan deviation for the laser power [13]. The deviation for averaging timescales of 10 seconds was below 0.1%.

Algorithm S3. SDE counts measurement

```
 1: procedure CONSOLE_DE(device_list, params, out)                              ▷ params ≡ parameters, out ≡ files
 2:     att_list ← device_list[0, 1, 2]                                                              ▷ List of attenuators
 3:     [pm, sw, pc] ← device_list[3, 4, 5]                    ▷ pm ≡ MPM, sw ≡ optical switch, pc ≡ polarization controller
 4:     [vsrc, counter] ← device_list[6, 7]                              ▷ vsrc ≡ voltage source, counter ≡ pulse counter
 5:
 6:     [attval, rngval] ← params[0, 1]                        ▷ attval ≡ attenuator value, rngval ≡ MPM range value
 7:     [vstop, vstep, vpol] ← params[2, 3, 4]        ▷ Voltage bias end-stop, step, and polarization optimization settings
 8:     [out_att, out_maxpol, out_minpol] ← out                                                       ▷ Output files
 9:
10:     N = 10                                                                             ▷ Number of counter readings
11:     att_list.set_att(attval)                                                              ▷ Set attenuators to attval
12:     vsrc.set_volt(0)                                                                        ▷ Set voltage bias to 0 V
13:
14:     [out_maxpol, out_minpol].write('# Dark Counts')                                  ▷ Start recording dark counts
15:     sw.set_route('monitor_port')
16:     att_list.disable()
17:     for vval ← 0 to vstop by vstep do
18:         vsrc.set_volt(vval)
19:         for i ← 1 to N do                                                                        ▷ Iterate N times
20:             counts = counter.get_counts()
21:             [out_maxpol, out_minpol].write(vval, counts)                          ▷ Count for 1 sec., write to files
22:     vsrc.set_volt(0)
23:
24:     att_list.enable()
25:     sw.set_route('detector_port')
26:     vsrc.set_volt(vpol)                                                   ▷ Set voltage bias for polarization optimization
27:     maxpol_settings ← maximize_counts(pc, counter, out_maxpol)
28:     minpol_settings ← minimize_counts(pc, counter, out_minpol)
29:     vsrc.set_volt(0)
30:
31:     out_maxpol.write('# Maxpol light counts')                                  ▷ Start recording 'maxpol' counts
32:     pc.set(maxpol_settings)
33:     for vval ← 0 to vstop by vstep do
34:         vsrc.set_volt(vval)
35:         for i ← 1 to N do                                                                        ▷ Iterate N times
36:             counts = counter.get_counts()
37:             out_maxpol.write(vval, counts)                                       ▷ Count for 1 sec., write to files
38:     vsrc.set_volt(0)
39:
40:     out_minpol.write('# Minpol light counts')                                  ▷ Start recording 'minpol' counts
41:     pc.set(minpol_settings)
42:     for vval ← 0 to vstop by vstep do
43:         vsrc.set_volt(vval)
44:         for i ← 1 to N do                                                                        ▷ Iterate N times
45:             counts = counter.get_counts()
46:             out_minpol.write(vval, counts)                                       ▷ Count for 1 sec., write to files
47:     vsrc.set_volt(0)
48:
49:     sw.set_route('monitor_port')
50:     CONSOLE_CAL(pm, att_list, attval, rngval, out_att)                         ▷ Attenuator calibration (see algorithm S2)
```
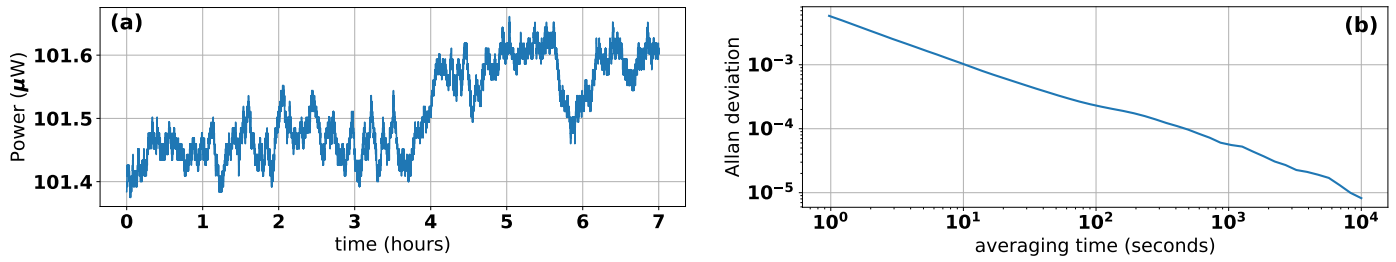
3. POLARIZATION SENSITIVITY MEASUREMENT

In order to ensure that we were sampling all input polarization states on the Bloch sphere, we replaced the MCP-01 all-fiber polarization controller with an HP8169A free-space polarization controller. This instrument out-coupled the

Fig. S8. (a) The power meter reading after 17 hours of equilibration time, sampled at approximately 4.118 Hz. (b) Allan deviation plot on a log-log scale for the same. Allan deviation for 10-second averaging is $= 9.28e - 4$.

fiber input to a free-space beam that is transmitted successively through a linear polarizer, a quarter-wave plate, and a half-wave plate, and then coupled back into an output fiber port. The three optical components are mounted on motorized rotational mounts, allowing for complete control of the polarization state of the output mode. Unlike the all-fiber polarization controller, this instrument had a polarization-setting dependent transmission loss, which had to be measured using both the CPM and MPM by splicing the detector-port to the fiber coupled to the CPM. The free-space nature of the instrument introduced significant drift on an hour timescale. Therefore this polarization-settings-dependent transmission was estimated for each of the three DUT counts-based measurements in turn.

Figure S9 plots the raw counts, the polarization-settings dependent transmission loss (expressed as 'pmratio'), and the loss-normalized counts for all three DUTs in three separate rows. No attempt at smoothing the data was made when estimating polarization sensitivity in this method.

DATA AND CODE AVAILABILITY STATEMENT

All of the data gathered for this manuscript and the `python` code used to implement the processing described in this document has been made available as a `zip`-archive file (SHA-1 `91599a67964d30b695b50b4719985533e98869a0`), along with a digital signature from the primary author (gpg fingerprint: `CC49 3CCF 1104 0DC7 36C4 5A7C E4E5 0022 5ED1 7577`). These files are available as supplementary materials through the journal, and copies of the same can be provided by the authors upon request.

DISCLAIMER

Identification of commercial instruments in this document does not imply recommendation or endorsement by the National Institute of Standards and Technology.

REFERENCES

1. D. V. Reddy, R. R. Nerem, S. W. Nam, R. P. Mirin, and V. B. Verma, "Superconducting nanowire single-photon detectors with 98% system detection efficiency at 1550 nm," Optica **7**, 1649 (2020).
2. A. N. McCaughan, A. N. Tait, S. M. Buckley, D. M. Oh, J. T. Chiles, J. M. Shainline, and S. W. Nam, "Phidl: Python-based layout and geometry creation for nanolithography," J. Vac. Sci. & Technol. B **39**, 062601 (2021).
3. R. Baghdadi, E. Schmidt, S. Jahani, I. Charaev, M. G. W. Müller, M. Colangelo, D. Zhu, K. Ilin, A. D. Semenov, Z. Jacob, and et al., "Enhancing the performance of superconducting nanowire-based detectors with high-filling factor by using variable thickness," Supercond. Sci. Technol. **34**, 035010 (2021).
4. J. R. Clem and K. K. Berggren, "Geometry-dependent critical currents in superconducting nanocircuits," Phys. Rev. B **84** (2011).
5. M. Jönsson, R. Vedin, S. Gyger, J. A. Sutton, S. Steinhauer, V. Zwiller, M. Wallin, and J. Lidmar, "Current crowding in nanoscale superconductors within the ginzburg-landau model," (2021). ArXiv:2112.05443.
6. A. J. Miller, A. E. Lita, B. Calkins, I. Vayshenker, S. M. Gruber, and S. W. Nam, "Compact cryogenic self-aligning fiber-to-detector coupling with losses below one percent," Opt. Express **19**, 9102 (2011).
7. P. Hu, H. Li, L. You, H. Wang, Y. Xiao, J. Huang, X. Yang, W. Zhang, Z. Wang, and X. Xie, "Detecting single infrared photons toward optimal system detection efficiency," Opt. Express **28**, 36884 (2020).
8. J. Chang, J. W. N. Los, J. O. Tenorio-Pearl, N. Noordzij, R. Gourgues, A. Guardiani, J. R. Zichi, S. F. Pereira, H. P. Urbach, V. Zwiller, and et al., "Detecting telecom single photons with $99.5^{+0.5}_{-2.07}$% system detection efficiency and high time resolution," APL Photonics **6**, 036114 (2021).
9. F. Marsili, V. B. Verma, J. A. Stern, S. Harrington, A. E. Lita, T. Gerrits, I. Vayshenker, B. Baek, M. D. Shaw, R. P. Mirin, and et al., "Detecting single infrared photons with 93% system efficiency," Nat. Photonics **7**, 210–214 (2013).
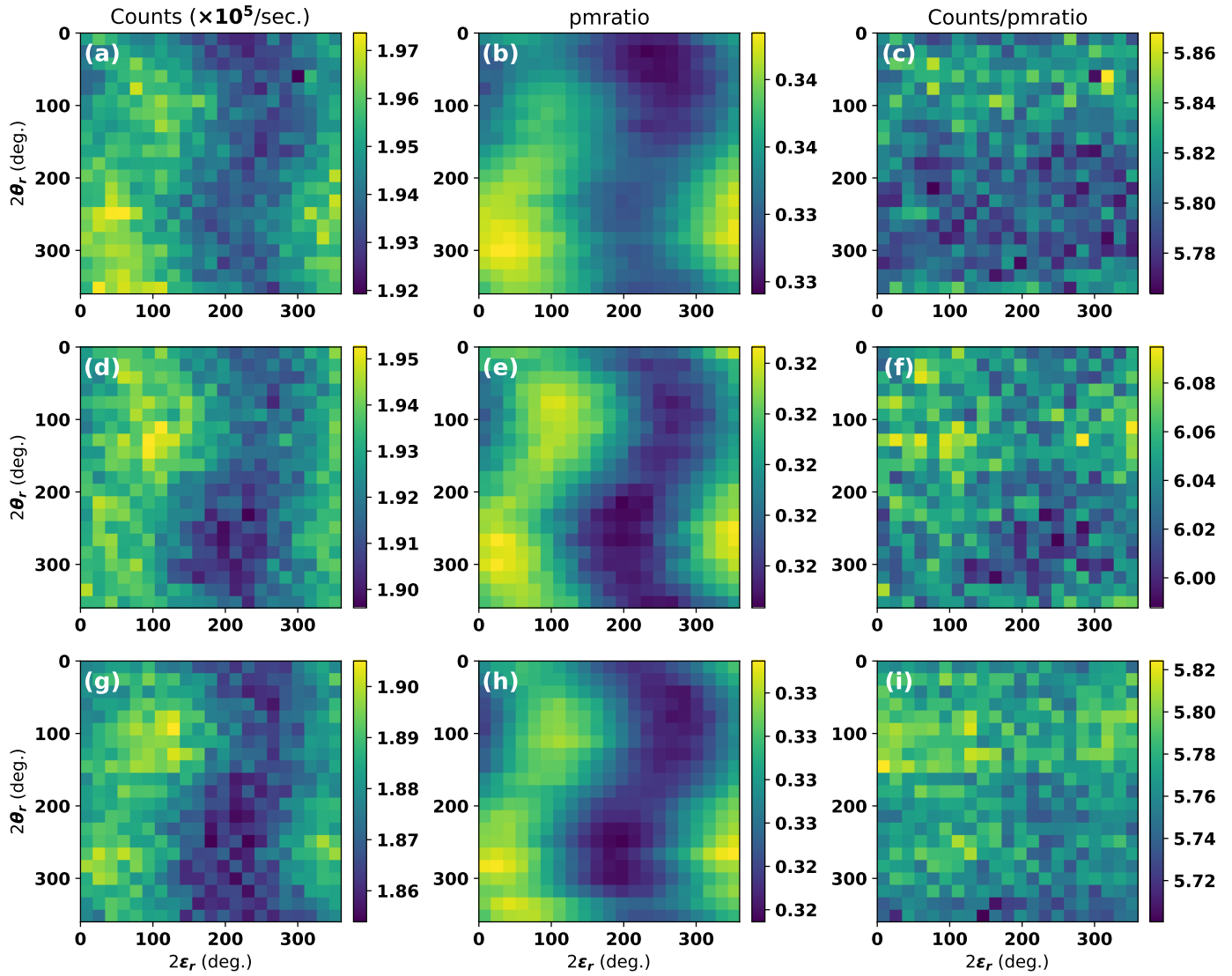
Fig. S9. The raw net counts (light counts - dark counts) (a, d, g), the power-meter ratio or transmission factor (b, e, h), and the transmission-factor corrected count rate (c, f, i) for detectors D1 (a, b, c), D2 (d, e, f), and D3 (g, h, i) over various polarization settings on the `HP8169A` free-space polarization controller. The max/min polarization sensitivities are (c) 1.018, (f) 1.018, and (i) 1.021. The standard uncertainty for all three is ±0.008.

10. T. Gerrits, A. Migdall, J. C. Bienfang, J. Lehman, S. W. Nam, J. Splett, I. Vayshenker, and J. Wang, "Calibration of free-space and fiber-coupled single-photon detectors," Metrologia **57**, 015002 (2019).

11. I. Vayshenker, S. Yang, and R. Swafford, "Nonlinearity of high-power optical fiber power meters at 1480 nm," Appl. Opt. **45**, 1098 (2006).

12. I. Vayshenker, S. Yang, X. Li, T. R. Scott, and C. L. Cromer, "Optical fiber power meter nonlinearity calibrations at NIST," NIST Special Publ. pp. 250–256 (2000).

13. T. Witt, "Using the allan variance and power spectral density to characterize dc nanovoltmeters," IEEE Transactions on Instrumentation Meas. **50**, 445–448 (2001).